Baroclinic Structure of the Abyssal Circulation and the Role of Meridional Topography*

JOSEPH PEDLOSKY AND DAVID C. CHAPMAN

Department of Physical Oceanography, Woods Hole Oceanographic Institution, Woods Hole, Massachusetts

(Manuscript received 20 March 1992, in final form 17 July 1992)

ABSTRACT

A simple linear model of the abyssal circulation is studied in which a north–south topographic slope influences the interior and boundary-layer flow. As in an earlier study, the reversals of the meridional velocity in the abyssal interior are related to the longitudinal variation of upwelling into the main thermocline.

When the topography slopes in the anti-β sense (down to the north in the northern hemisphere) an *eastern* boundary current appears regardless of the magnitude of the slope. If the slope is weak, the eastern boundary current is broad and bottom trapped. As the slope becomes steeper, the current narrows and stretches vertically. At a critical value of the slope, for which the barotropic potential vorticity gradient changes sign, the eastern boundary current metamorphoses into a modified Munk layer.

For all values of the slope, a system of broad, baroclinic western boundary currents exist whose effects reach rather far into the interior.

1. Introduction

The classical theory of Stommel and Arons (1960a,b) for the abyssal circulation of the world's oceans represents the abyssal waters by a single layer of homogeneous fluid in a basin with a flat bottom. The abyssal motion in the interior of the basin, distant from swift boundary currents, is forced by a hypothesized large-scale upwelling into the regions of the lower main thermocline. Consequent to strictly geostrophic, barotropic dynamics, the meridional flow in the interior of the basin is always poleward regardless of the distribution of the sources of abyssal water provided by geographically specific sinking zones where cold abyssal water is made. The independence of the direction of the interior flow from the distribution of deep-water sources is one of the least intuitive and yet most powerful results of the theory. Its power lies in providing a theory for the interior flow that is largely decoupled from the dynamics of boundary current regions.

In an attempt to deal with the observed baroclinic structure of the abyssal circulation, one of us (Pedlosky 1992, hereafter P92) has suggested that under realistic parameter settings the baroclinic response of the abyssal waters to upwelling could dominate the barotropic response especially when the upwelling, as might be expected from elementary arguments (first put forward by Stommel and Arons themselves), varies strongly spatially and, in particular, is enhanced in the eastern parts of the oceanic basins where the thermocline's vertical temperature gradient is strongest. The theory described in P92 displays a weak poleward barotropic velocity dominated in the western ocean by the baroclinic response to the localized upwelling, which has propagated westward under the influence of the planetary vorticity gradient β. The strong baroclinic response carries no *net* meridional transport, and this result has been put forward as a possible mechanism for the observed baroclinic layering of the interior circulation which, in sympathy with the basic ideas of the classical theory, is relatively insensitive to the distribution of formation regions of cold water.

The model used in P92 is an idealized, highly simplified one. The principal simplification is a linearization of the density field about a known "standard" density structure characterized by a given buoyancy frequency $N(z)$. The thermodynamics is similarly idealized through the use of a linear partial differential equation for the weak density anomaly around the basic structure. A second important simplification is the unrealistic absence of topographic effects. A flat bottom allows a simple decomposition between a barotropic mode which carries *all* the transport and is independent of the stratification and an infinite set of vertical baroclinic modes each of which carries *no* horizontal transport.

In this paper, we report on an extension of the model used in P92 to one in which the effects of bottom topography are included. Thus it shares with Pedlosky's earlier study all the deficiencies of the rudimentary treatment of the thermodynamics and determination of density. It can therefore be expected that horizontal

* Woods Hole Oceanographic Institution Contribution No. 8094.

Corresponding author address: Dr. David C. Chapman, Woods Hole Oceanographic Institution, Woods Hole, MA 02543.

advection of density, ignored in the model, might quantitatively alter some of our results.

The focus of our attention in this paper is, however, the role of topography in the dynamics of a continuously stratified model of the abyssal circulation. It is well known that for a *barotropic* fluid there is a precise dynamic analogy between the planetary vorticity gradient β and the equivalent contributor to the background potential vorticity gradient due to topography,

$$\frac{f}{H}\frac{\partial h}{\partial y}$$

[or more generally $(f/H)\nabla h$], where h is the height of the topography above the bottom, H is the thickness of the abyssal layer, f is the Coriolis parameter, and y is the meridional coordinate, positive northward. In a layered model of the ocean circulation, the analogy would still hold for the bottom layer covering the topography. It is much less clear what the appropriate equivalence is for a continuously stratified fluid for which the sloping lower boundary explicitly affects only the kinematic bottom boundary condition. One of the principal goals of the present study is an examination of how the results for the interior circulation are altered by the presence of a meridional slope in the bottom depth. For technical reasons described later we are, for now, avoiding the equally interesting question of zonally sloping topography for which case, roughly speaking, the effective potential vorticity gradient twists with depth.

An important consequence of the presence of the topographical slope is that the modal decomposition, though still possible, no longer denies to the higher baroclinic modes net, vertically integrated transport. Hence, considerable care must be taken in delineating and interpreting the character of the baroclinic portion of the solution when topography is present.

Perhaps one of the most pressing oceanographic questions presented by the topographic effect concerns the *position* of the transport-carrying boundary currents. For a flat bottom, such boundary currents must be on the western side of the ocean. As we know, the position of the boundary current depends on the sign of the potential vorticity gradient. In a barotropic fluid, the overall ambient potential vorticity gradient can be reversed when

$$\frac{fh_y}{H} < -\beta, \tag{1.1}$$

that is, when the bottom of the ocean is sloping downward towards the pole strongly enough to reverse the β effect. The degree to which (1.1) defines a critical bottom slope for reversal is unclear for a continuously stratified fluid.

For a homogeneous fluid, satisfaction of (1.1) would imply a reversal of roles of eastern and western boundaries of the basin with the appearance of strong currents on the eastern sides of the basin. This has been appealed to as a possible cause for the transposition of the abyssal boundary current in the tropical latitudes of the North Atlantic (Warren 1981). We shall present results that indicate that for a continuously stratified fluid, the situation is dynamically much richer. In particular, we show that *no* critical slope for transposition exists in the sense that for *any* negative[1] slope some net meridional transport can be expected to be carried in a boundary layer on the *eastern* side of the basin. However, regardless of the size of the slope, a system of baroclinic, mass transporting boundary currents is also always found on the western side of the basin.

In the model described in this paper, for which the topography has only a meridional variation, only the depth and zonal coordinates enter as explicit independent variables. We exploit this fact by considering, explicitly, only zonal slices of the full circulation problem and let the meridional variation be carried parametrically. This is only made possible by ignoring, for the most part, that part of the boundary layer physics that relates the boundary layer net transports to the distribution of sources. Our model is consequently, in truth, largely limited to the structure of the recirculating portion of the abyssal flow insofar as the transports of the currents are concerned. However, the dynamics, spatial structure, and most important, the position of the boundary currents are fully revealed by our simple model. A more elaborate, completely three-dimensional model knitting together the boundary currents and the deep-water sources is a subject of our future work.

2. The model (interior)

The model and its dynamics are, with the exception of the addition of a meridional topographic slope, the same as in P92. Using standard terminology and local Cartesian coordinates, the motion is considered to be geostrophic, hydrostatic, and incompressible; that is,

$$fv = \frac{1}{\rho_0}\frac{\partial p}{\partial x},$$

$$fu = -\frac{1}{\rho_0}\frac{\partial p}{\partial y}, \tag{2.1a,b}$$

where f is the variable Coriolis parameter, ρ_0 is a constant density typical of the abyss, and p is the pressure anomaly which drives the motion. The hydrostatic relation is

$$\rho g = -\frac{\partial p}{\partial z}, \tag{2.2}$$

[1] Falling prey to Northern Hemisphere chauvinism, we define a positive (negative) slope as one for which $f(\partial h/\partial y)$ is positive (negative).

in which ρ is the density anomaly related to the motion. As in P92, the equation for the density anomaly is the linear equation

$$-w\left\{\frac{N^2}{g}\right\} = \frac{\kappa}{\rho_0}\frac{\partial^2\rho}{\partial z^2}, \tag{2.3}$$

where

$$\frac{N^2}{g} = -\frac{1}{\rho_0}\frac{\partial\bar{\rho}}{\partial z},$$

where $\bar{\rho}(z)$ is the full background density field and κ is the vertical mixing coefficient for density. Throughout, we will take N^2 a constant for simplicity. The condition of incompressibility is

$$\frac{\partial u}{\partial x} + \frac{\partial v}{\partial y} + \frac{\partial w}{\partial z} = 0. \tag{2.4}$$

The basin is idealized to lie between constant meridians at $x = x_w$ and x_e at its western and eastern ends, respectively. Within boundary layers near either $x = x_w$ or x_e, we anticipate that equations (2.1b) and (2.3) will be supplemented by mixing terms on the right-hand sides of the form

$$A\frac{\partial^2 v}{\partial x^2} \quad \text{and} \quad \frac{\kappa_H}{\rho_0}\frac{\partial^2\rho}{\partial x^2},$$

respectively.

At the upper boundary of our domain, which we take to represent the top of the abyss and the base of the permanent thermocline, we specify the vertical velocity, namely,

$$w = w_*(x, y), \quad z = 0, \tag{2.5}$$

while with little loss in generality we set the density *anomaly* to zero there

$$\rho = 0, \quad z = 0. \tag{2.6}$$

At the lower boundary, at $z = -H$, the anomalous density is again set to zero:

$$\rho = 0, \quad z = -H, \tag{2.7}$$

while the kinematic boundary condition yields

$$w = v\frac{\partial h}{\partial y}, \quad z = -H. \tag{2.8}$$

Consistent with the linearization of the density field, we apply (2.7) and (2.8) at the constant mean depth H, although in the x–z slice model developed here, H may equally as well be interpreted as the *local* depth.

Geostrophy and incompressibility yield the Sverdrup relation

$$\beta v = f\frac{\partial w}{\partial z}, \tag{2.9}$$

where $\beta = df/dy$, which with the density equation (2.3), the hydrostatic equation (2.2), and again, the geostrophic equation for v yields the governing equation for the interior in the form:

$$\frac{\partial^4 p}{\partial z^4} = \frac{\beta N^2}{\kappa f^2}\frac{\partial p}{\partial x}. \tag{2.10}$$

The boundary conditions at $z = 0$ and $z = -H$ become

$$\frac{\partial p}{\partial z} = 0, \quad z = 0, -H$$

$$\frac{\partial^3 p}{\partial z^3} = \rho_0\frac{N^2}{\kappa}w_*, \quad z = 0$$

$$\frac{\partial^3 p}{\partial z^3} = \frac{N^2}{\kappa f^2}\left(\frac{\partial p}{\partial x}f\frac{\partial h}{\partial y}\right), \quad z = -H. \tag{2.11a,b,c}$$

Equation (2.10) implies a characteristic vertical scale d for the motion equal to d_L where

$$d_L = \left[\frac{\kappa f^2}{\beta N^2}(x_e - x_w)\right]^{1/4} \tag{2.12}$$

is the Stommel–Veronis (1957) depth. An implicit assumption of our analysis is that d_L is $O(H)$.

On the lateral boundary of the basin the natural boundary conditions are no normal flow and, say, no slip. Now as remarked earlier, (2.10) and (2.11) yield a problem explicitly dependent on only x and z. A complete application of the no normal flow condition would introduce $\partial p/\partial y$ into the problem and thus turn the problem into a three-dimensional differential system. This would draw us into a complex discussion of the local strength of the boundary currents and its connection to specified sources of deep water on the perimeter of the basin. We prefer to stick to the simpler problem suggested above and replace the normal flow condition with the *stronger* condition of vanishing pressure anomaly on $x = x_e$ and x_w. This restricts us, to the extent that the meridional velocity is geostrophic, to describing a purely recirculating flow, but the simplifications seem to us to outweigh the limitations at this stage. As we shall see, such boundary conditions are sufficient to reveal the subtle role played by topography in determining the structure and position of the boundary currents. At the same time, we do not anticipate that the interior structure will depend qualitatively on the relationship between the boundary currents and the sources. Thus our model formulation is completed with the conditions

$$p = \frac{\partial p}{\partial x} = 0 \quad \text{on} \quad x = x_e \quad \text{and} \quad x_w. \tag{2.13}$$

3. The interior model solution

In the basin's interior where (2.10) and (2.11) apply, a solution may be found in terms of the normal modes

of the following eigenvalue problem. We introduce the set of eigenfunctions $\phi_n(z)$ that satisfy

$$\frac{d^4\phi_n}{dz^4} - \frac{\lambda_n^4}{H^4}\phi_n = 0 \tag{3.1}$$

subject to

$$\frac{\partial^3\phi_n}{\partial z^3} = \frac{\partial\phi_n}{\partial z} = 0, \quad z = 0 \tag{3.2}$$

$$\frac{\partial\phi_n}{\partial z} = 0, \quad z = -H \tag{3.3a}$$

$$\frac{\partial^3\phi_n}{\partial z^3} = \frac{\lambda_n^4}{H^3 B}\phi_n, \quad z = -H. \tag{3.3b}$$

The parameter B is our measure of the relative importance of β with respect to the bottom slope, namely,

$$B = \frac{\beta H}{f(\partial h/\partial y)}. \tag{3.4}$$

The solution of (3.1) subject to (3.2) and (3.3) is

$$\phi_n = \cos\left(\lambda_n \frac{z}{H}\right) + \frac{\sin\lambda_n}{\sinh\lambda_n}\cosh\left(\lambda_n \frac{z}{H}\right), \tag{3.5}$$

where λ_n is a solution of the transcendental equation:

$$\tan\lambda_n = -\frac{\lambda_n \tanh\lambda_n}{\lambda_n + 2B\tanh\lambda_n}. \tag{3.6}$$

When the bottom is flat ($B \to \infty$) the eigenvalues λ_n are multiples of π and the eigensolutions form the cosine series used in P92. For finite B a bottom-trapped adjustment to the eigenfunction is represented by the second term in (3.5). Note that $\lambda = 0$, corresponding to the eigenfunction $\phi_0 = 1$, is always allowed. As $B \to -1$, at which value the β effect for a barotropic fluid would be canceled by the bottom slope,

$$\lambda_1 \to 2.59(1 + B)^{1/4} \tag{3.7}$$

and hence coalesces with λ_0.

For general B the orthogonality rule for the set ϕ_n is

$$\int_{-H}^{0} \phi_n\phi_m dz + \frac{H}{B}\phi_m(-H)\phi_n(-H) = 0, \quad m \neq n. \tag{3.8}$$

Since $\phi = 1$ is an eigenfunction corresponding to $\lambda_n = 0$, it follows that for all $n > 0$ ($\lambda_n \neq 0$)

$$\int_{-H}^{0} \phi_n dz = -\frac{H}{B}\phi_n(-H) \neq 0, \tag{3.9}$$

so that *all the higher baroclinic modes have a nonzero vertical average as long as B is finite,* that is, as long as $\partial h/\partial y \neq 0$.

Any function, $p(x, y, z)$ for example, can be expanded in the series

$$p = \sum_{n=0}^{\infty} P_n\phi_n(z), \tag{3.10}$$

with

$$P_n = \frac{1}{C_n}\left[\int_{-H}^{0} p\phi_n dz + \frac{H}{B}p(-H)\phi_n(-H)\right], \tag{3.11}$$

where

$$C_n = \int_{-H}^{0}\phi_n^2 dz + \frac{H}{B}\phi_n^2(-H)$$

$$= \frac{H}{2}\left\{1 + \sin^2\lambda_n\left[\frac{1}{\sinh^2\lambda_n} + \frac{2B}{\lambda_n^2}\right]\right\}, \quad \lambda_n \neq 0. \tag{3.12a}$$

For $\lambda_n = 0$, we take $\phi_0 = 1$ and then it follows directly from (3.8) that

$$C_0 = H\{1 + B^{-1}\}, \quad \lambda_n = 0. \tag{3.12b}$$

If (2.10) is multiplied by ϕ_n, integrated over the interval $(-H, 0)$, and use is made of the boundary conditions and the projection law (3.10), we obtain for P_n the ordinary differential equation

$$\frac{\partial P_n}{\partial x} - \frac{\lambda_n^4\kappa f^2}{H^4\beta N^2}P_n = \frac{\phi_n(0)f^2}{C_n\beta}\rho_0 w_*(x). \tag{3.13}$$

The meridional velocity can similarly be expanded as

$$v = \sum_{n=0}^{\infty} V_n\phi_n(z), \tag{3.14}$$

where

$$V_n = \frac{1}{\rho_0 f}\frac{\partial P_n}{\partial x}. \tag{3.15}$$

For the eigenmode corresponding to $\lambda = 0$ ($n = 0$), it follows from (3.13) that the solution for V_0 is *local* in x. That is, it depends only upon the *local* value of the upwelling w_*. Since $\phi_0 = 1$, it follows directly from (3.12) and (3.13) that

$$V_0 = fw_* \Big/ H\left\{\beta + \frac{f}{H}\frac{\partial h}{\partial y}\right\}. \tag{3.16}$$

This would be the meridional Sverdrup flow for a *barotropic* fluid in which the planetary vorticity gradient is modified by the bottom slope. It must not be thought that this is the solution for the vertically averaged meridional transport. As (3.9) shows, *all* the higher modes in the sum (3.14) also carry a net meridional transport.

The formal solution for the interior can be obtained from (3.13) as

$$P_n = -\int_x^{x_e} \frac{\phi_n(0) f^2 \rho_0}{C_n \beta} w_*(x') e^{-\alpha_n(x'-x)} dx' + P_n(x_e) e^{-\alpha_n(x_e - x)}, \quad (3.17)$$

where

$$\alpha_n = \left(\frac{\lambda_n}{H}\right)^4 \frac{\kappa f^2}{\beta N^2} \quad (3.18)$$

so that

$$v = \frac{f w_*}{H\{\beta + (f/H)\partial h/\partial y\}} + \sum_{n=1}^{\infty} \frac{f}{\beta C_n} \phi_n(0)\phi_n(z)\left[w_* - \int_x^{x_e} \alpha_n e^{-\alpha_n(x'-x)} w_* dx' \right] + \sum_{n=1}^{\infty} \frac{\alpha_n}{\rho_0 f} \phi_n(z) P_n(x_e) e^{-\alpha_n(x_e - x)}. \quad (3.19)$$

The functions $P_n(x_e)$ are, so far, arbitrary. If we were to assume that the interior flow satisfies the boundary condition $p = 0$ on $x = x_e$, then $P_n(x_e)$ would be zero. Normally, we expect the interior solution, governed by Sverdrup dynamics, to do just that. However, the presence of bottom topography introduces the possibility that the eastern and western boundaries could dynamically reverse identities. As in the classical homogeneous case, this can only be decided, and the interior solution can only be finally determined, when an analysis of the sidewall boundary layers is completed.

4. Sidewall boundary layers

Near $x = x_e$ and x_w, sidewall boundary layers are required to correct the interior solution so that the boundary conditions (2.13) can be satisfied. If we write each variable, for example, p, as the sum of the interior solution plus a boundary-layer *correction* function, then

$$p = p_I(x, z) + \tilde{p}(x, z). \quad (4.1)$$

In (4.1), the I subscripted variable refers to the interior functions derived in the previous section. The tilde variables are corrections that exponentially go to zero outside the narrow boundary layers near $x = x_e$ and x_w. The linearity of the basic dynamics then allows us to write the equations for the correction variables as

$$\tilde{v} = \frac{1}{\rho_0 f}\frac{\partial \tilde{p}}{\partial x},$$

$$\tilde{u} = -\frac{1}{\rho_0 f}\frac{\partial \tilde{p}}{\partial y} + \frac{A}{f}\frac{\partial^2 \tilde{v}}{\partial x^2}$$

$$\frac{\partial \tilde{u}}{\partial x} + \frac{\partial \tilde{v}}{\partial y} + \frac{\partial \tilde{w}}{\partial z} = 0,$$

$$-\tilde{w}\frac{N^2}{g} = \frac{\kappa}{\rho_0}\frac{\partial^2 \tilde{\rho}}{\partial z^2} + \frac{\kappa_H}{\rho_0}\frac{\partial^2 \tilde{\rho}}{\partial x^2},$$

$$\frac{\partial \tilde{p}}{\partial z} = -\tilde{\rho} g. \quad (4.2a,b,c,d,e)$$

In (4.2) we have taken the meridional velocity to be geostrophic. This assumption is easily validated post hoc. The appearance of horizontal mixing of momentum and density in (4.2b and d) raises the differential order of the system and allows sidewall boundary layers to satisfy (2.13).

A single, master equation for $\tilde{p}$ can be derived from (4.2) as

$$\underset{①}{\frac{A}{f^2}\frac{\partial^4 \tilde{p}}{\partial x^4}} + \underset{②}{\frac{\kappa_H}{N^2}\frac{\partial^4 \tilde{p}}{\partial z^2 \partial x^2}} + \underset{③}{\frac{\kappa}{N^2}\frac{\partial^4 \tilde{p}}{\partial z^4}} - \underset{④}{\frac{\beta}{f^2}\frac{\partial \tilde{p}}{\partial x}} = 0, \quad (4.3)$$

where numbers, coding each term, are placed below. The issue that arises now is what balances, as a function of the parameters, are possible in (4.3). In the boundary layer, $\partial/\partial x = 0(1/l)$, where l is the boundary-layer scale. Since $l \ll (x_e - x_w)$ and the vertical scale d_L as defined by (2.12) is of order H, then ③ is always negligible with respect to ④ within the boundary layer.

Two possibilities remain. The first possibility is that term ① balances term ④, while term ② is negligible. This would lead to a boundary-layer scale

$$l = l_M = \left(\frac{A}{\beta}\right)^{1/3}, \quad (4.4)$$

which is the thickness of Munk's boundary layer, only here for a stratified fluid. To ignore ②, this balance requires

$$l_M \ll \left(\frac{A}{\kappa_H}\right)^{1/2} \frac{NH}{f}, \quad (4.5)$$

that is, that the stratification be so strong that (assuming $A \sim \kappa_H$) l_M is much less than a deformation radius.

It may seem paradoxical that the Munk balance, familiar to us from the dynamics of a homogeneous fluid, requires *strong* stratification. However, for the Munk balance to occur, vorticity production by stretching must be negligible and this requires either a homogeneous fluid of uniform depth *or* a strongly stratified fluid, for example, $l_M \ll$ deformation radius. Such a thin boundary layer is rather unlikely, and we prefer to follow Warren's (1981) suggested choice of parameters and instead consider the balance between ② and ④, which requires the inequality in (4.5) to be reversed. The boundary-layer scale that this balance yields is

$$l = l_B = \frac{\kappa_H f^2}{N^2 H^2 \beta} \gg l_M, \tag{4.6}$$

the inequality following from the reversal of (4.5).

We introduce the nondimensional boundary-layer variable

$$\xi = \frac{x}{l_B}$$

so that the boundary-layer equation now becomes

$$H^2 \frac{\partial^4 \tilde{p}}{\partial z^2 \partial \xi^2} - \frac{\partial \tilde{p}}{\partial \xi} = 0. \tag{4.7}$$

The appropriate boundary condition for (4.7) comes from the kinematic conditions on $z = 0$ and $z = -H$. For the correction functions

$$\tilde{w} = 0 \quad \text{on} \quad z = 0$$

$$\tilde{w} = \tilde{v} \frac{\partial h}{\partial y} \quad \text{on} \quad z = -H,$$

which translates to

$$\frac{\partial \tilde{p}}{\partial z} = 0, \quad z = 0$$

$$\frac{\partial^3 \tilde{p}}{\partial z \partial \xi^2} = \frac{1}{BH} \frac{\partial \tilde{p}}{\partial \xi}, \quad z = -H. \tag{4.8a,b}$$

The boundary-layer problem (4.7), (4.8) can be analyzed, as in the case of the interior, with the aid of an expansion in vertical modes. In the present case, we write

$$\tilde{p} = \sum_{n=0}^{\infty} \tilde{P}_n \psi_n(z), \tag{4.9}$$

where the $\psi_n(z)$ satisfy

$$\frac{\partial^2 \psi_n}{\partial z^2} + \frac{\nu_n^2}{H^2} \psi_n = 0, \tag{4.10}$$

subject to

$$\frac{\partial \psi_n}{\partial z} = 0 \quad \text{on} \quad z = 0$$

$$\frac{\partial \psi_n}{\partial z} = -\frac{\nu_n^2}{BH} \psi_n \quad \text{on} \quad z = -H. \tag{4.11a,b}$$

The eigensolutions are

$$\psi_n = \cos\left(\nu_n \frac{z}{H}\right), \tag{4.12a}$$

where the eigenvalue ν_n satisfies

$$\tan\nu_n = -\frac{\nu_n}{B}. \tag{4.12b}$$

A solution for which ν is entirely imaginary, that is,

$$\nu_0 = i\mu_0,$$

may also be sought for which

$$\psi_0 = \cosh\left(\mu_0 \frac{z}{H}\right), \tag{4.13a}$$

while

$$\tanh\mu_0 = -\frac{\mu_0}{B}. \tag{4.13b}$$

The transcendental equations for the eigenvalues ν_0, ν_n can be appreciated best by examining Fig. 1, where the curves for $\tan\nu$, $\tanh\mu_0$ are shown as well as the line $-(\nu/B)$ (for ν_n and μ_0) for values of B for which $B > 0$, $-1 < B < 0$, and $B < -1$. The intersection of the straight lines with $\tan\nu$ and $\tanh\mu_0$ give the possible eigenvalues.

For $B > 0$ the only intersections possible are with the $\tan\nu$ curves. That is, there is no solution corresponding to (4.13) for $B > 0$, and each vertical mode is trigonometric. These yield the intersections marked ○ in the figure. If the topography is strongly sloping in the anti-β sense so that $-1 < B < 0$, there are again only trigonometric solutions corresponding to the intersections marked □ in the figure. However, if the topography is *weakly* sloping ($B < -1$) in the anti-β sense (i.e., if the depth is increasing poleward), there are solutions of both (4.12) and (4.13) marked x in Fig. 1. In this case the single solution of (4.13) replaces the "missed" solution for $\nu < \pi/2$ that occurs for $-1 < B < 0$. As we shall see, this additional solution has

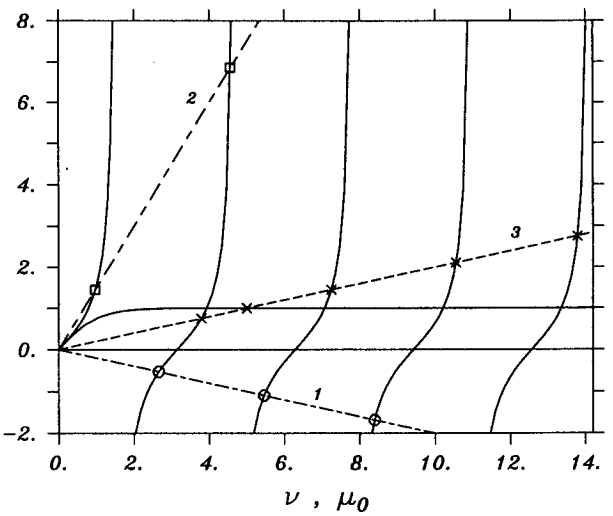

FIG. 1. The dispersion diagram for the boundary-layer modes. The curves for $\tan\nu$ and $\tanh\mu_0$ are shown. The intersection for the straight line $-\nu B^{-1}$ with each curve yields an eigenvalue. Line 1 shows the situation for $B^{-1} = (f/\beta H)\partial h/\partial y > 0$. Only intersections with $\tan\nu$ are possible. Line 2 shows the case for strong negative topography $B^{-1} < -1$. Again, only intersections of the line with the $\tan\nu$ curves are possible. For $-1 < B^{-1} < 0$ (i.e., large negative B), line 3 shows an intersection with the $\tanh\mu_0$ curve representing the appearance of the bottom-trapped mode on the eastern boundary.

dynamically important consequences. The additional solution (4.13a) is bottom trapped and exists *only when there is weak but nonzero negative topographic slope.*

The orthogonality conditions for the ψ_n are

$$\int_{-H}^{0} \psi_n \psi_m dz + \frac{H}{B}\psi_m(-H)\psi_n(-H) = 0, \quad m \neq n. \tag{4.14}$$

Again, since $\nu = 0$ is formally an eigenvalue corresponding to $\psi = 1$, it follows from (4.14) that

$$\int_{-H}^{0} \psi_n dz \neq 0;$$

that is, each mode will carry a net transport if $B^{-1} \neq 0$.

Use of the orthogonality rule allows us to substitute (4.9) into (4.7) to obtain

$$\nu_n^2 \frac{\partial^2 \tilde{P}_n}{\partial \xi^2} + \frac{\partial \tilde{P}_n}{\partial \xi} = 0 \tag{4.15}$$

for $\nu_n^2 > 0$. Solutions of (4.15) that are of boundary-layer character are of the form

$$\tilde{P}_n = \tilde{A}_n e^{-(\xi/\nu_n^2)}. \tag{4.16}$$

It is clear from (4.16) that these functions can only represent boundary-layer correction functions in the vicinity of the western boundary since they decay eastward. This is true regardless of the *sign* or *size* of the *topographic slope.*

It is important to note that the horizontal length scale of the boundary-layer correction increases like ν_n^2. Hence, vertically small-scale components will extend further from the boundary than deeper boundary-layer structures. The rule is "short and fat/tall and narrow."

For the solution for which $\nu_0 = i\mu_0$ (4.15) becomes

$$\mu_0^2 \frac{\partial^2 \tilde{P}_0}{\partial \xi^2} - \frac{\partial \tilde{P}_0}{\partial \xi} = 0, \tag{4.17}$$

the appropriate solution for which is

$$\tilde{P}_0 = \tilde{A}_0 e^{\xi/\mu_0^2}. \tag{4.18}$$

Hence, this function can serve as a boundary-layer correction function only near the *eastern* boundary of the basin as it decays exponentially westward and it exists only for *weak, negative* topographic slopes, that is, $B < -1$. Indeed, we can infer from (4.13b) and Fig. 1 that as the slope gets weaker, μ_0 increases so that the solution (4.18) becomes increasingly broad and bottom trapped. On the other hand, as $B \to -1$, $\mu_0 \to 0$, and this solution becomes increasingly narrow and tall.

To complete the picture of the boundary-layer structure we must examine the solution corresponding to the zero eigenvalue more carefully. It follows from (4.15) that for $\nu_n = 0$ [which is always a solution of (4.12b)], the boundary-layer equation becomes singular. This reflects that if $\tilde{p}$ is essentially independent of z (as for $\nu_n = 0$), the balance in the master equation between terms ② and ④ no longer holds. When $\tilde{p}$ is weakly dependent on z, term ① becomes important and ② loses its dominance even though the inequality required by (4.5) (that is, its reversal) obtains.

A more accurate representation of the nearly z-independent mode can be obtained from (4.3). Writing

$$\eta = \frac{x}{l_M}, \quad \zeta = \frac{z}{H}, \tag{4.19}$$

neglecting only term ③ in (4.3), integrating once in η, and using the condition that $\tilde{p}$ vanish for large η, we have

$$\frac{\partial^3 \tilde{p}}{\partial \eta^3} + \frac{l_B}{l_M}\frac{\partial^3 \tilde{p}}{\partial \zeta^2 \partial \eta} - \tilde{p} = 0, \tag{4.20}$$

while

$$\frac{\partial \tilde{p}}{\partial \zeta} = 0, \quad \zeta = 0$$

$$\frac{l_B}{l_M}\frac{\partial^2 \tilde{p}}{\partial \zeta \partial \eta} = \frac{1}{B}\tilde{p}, \quad \zeta = -1, \tag{4.21a,b}$$

where, by (4.6) $l_B/l_M \gg 1$. The consistent solution of (4.20) in this limit can be found as

$$\tilde{p} = \tilde{p}_0(\eta) + \frac{\zeta^2}{2}\frac{l_M}{l_B}\tilde{p}_1(\eta) + O\left(\frac{l_M}{l_B}\right)^2 + \cdots, \tag{4.22}$$

which when inserted in (4.20) yields

$$\frac{\partial^3 \tilde{p}_0}{\partial \eta^3} + \frac{\partial \tilde{p}_1}{\partial \eta} - \tilde{p}_0 = 0, \tag{4.23a}$$

while (4.21b) yields

$$\frac{\partial \tilde{p}_1}{\partial \eta} = -\frac{1}{B}\tilde{p}_0. \tag{4.23b}$$

Combining the preceding equations yields

$$\frac{\partial^3 \tilde{p}_0}{\partial \eta^3} - \left(1 + \frac{1}{B}\right)\tilde{p}_0 = 0. \tag{4.24}$$

This is simply the equation for the Munk layer in which β is modified by topography so that the effective β is $\beta + (f/H)\partial h/\partial y$. Thus for this mode *alone,* when (4.6) holds, there exists a critical value of B, that is, $B = -1$, for which the Munk layer switches sides from western to eastern walls.

It is useful at this point to recapitulate the anticipated boundary-layer structure on the basis of the previous arguments. A schematic summary is shown in Fig. 2. For $f(\partial h/\partial y) > 0$, that is, when the topography introduces a contribution to the planetary vorticity gradient that has the same sign as β, all boundary-layer structure that we have described is found near the western boundary (Fig. 2a). This structure consists of a modified Munk layer with a thickness l'_M,

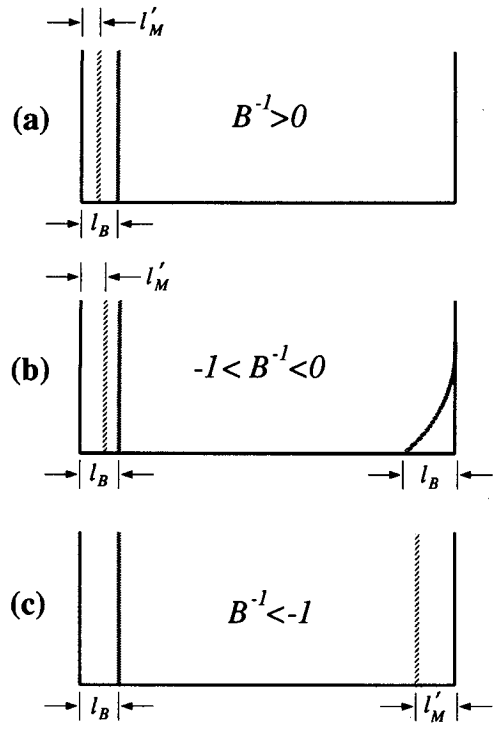

FIG. 2. A schematic displaying the position of the principal boundary-layer structures for the three parameter regimes $B^{-1} > 0$, $-1 < B^{-1} < 0$, $B^{-1} < -1$. The symbols are defined in the text.

$$l'_M = \left(\frac{A}{\beta\{1 + (1/B)\}}\right)^{1/3}, \tag{4.25}$$

and a vertical structure that is nearly z independent. In addition, there is a baroclinic structure, given by (4.12a), whose horizontal scale is for each mode

$$l_B \nu_n^2 = \frac{\kappa_H f^2}{N^2 H^2 \beta} \nu_n^2. \tag{4.26}$$

Note again that the higher vertical modes are broader. This boundary-layer structure is largely independent of topography although the ν_n depends quantitatively on B. Although this part of the structure is baroclinic, *each mode carries a net meridional transport.*

When the slope reverses but is still small so that

$$-1 < B^{-1} = \frac{f\,\partial h/\partial y}{\beta H} < 0, \tag{4.27}$$

the Munk layer becomes broader but remains on the western wall of the basin (Fig. 2b). The trigonometric modes [(4.12), (4.16)] also remain nestled against the western boundary. Reference to Fig. 1 shows, however, that the lowest trigonometric mode is lost. It is replaced by a bottom-trapped boundary-layer mode [(4.13), (4.18)] on the *eastern* boundary that exists only in the range given by (4.27). For very small topography this boundary layer is highly bottom-trapped and broad. As the negative slope increases in magnitude, the layer narrows and becomes less bottom trapped. That is, it tends to become z independent as $B \to -1$.

As the slope continues to steepen past the point $B = -1$, the bottom-trapped mode on the eastern wall disappears and is replaced by the Munk layer which, from (4.24), now switches sides from west to east as the *barotropic* potential vorticity gradient changes sign (Fig. 2c). The baroclinic trigonometric modes, however, are still present on the *western* side of the basin and still carry a net meridional transport. Thus, for all negative slopes, no matter what the magnitude, we anticipate transport-carrying boundary layers on *both eastern and western sides of the basin.*

We have described the transition with diminishing B as a sequence of parametric alterations. However, given that the boundary-layer equations carry y only parametrically, the transition of the boundary-layer character we have just described can be anticipated if the slope instead changes geographically. The transposition of the structure from a purely western boundary layer to one involving both boundaries can be expected to occur as the slope changes smoothly from positive to negative. We do not expect, though, to see a situation where the boundary-layer structure is present *only* on the eastern boundary since the baroclinic modes are sensitive primarily to the internal potential vorticity gradient due to β and therefore always remain in the west.

For completeness, as Warren (1981) remarks, the boundary-layer structure previously described must be supplemented by a very thin layer whose width is of the order of the deformation radius

$$l_D = \frac{NH}{f}, \tag{4.28}$$

when the inequality (4.6) applies. The balance ① − ② in (4.3) yields the scale given by (4.28). This sublayer always appears on both eastern and western boundaries. Its purpose is to help satisfy the no-slip condition and to transfer mass vertically in the boundary layer. It can be shown that it does not transport mass meridionally to any significant degree.

When $B > 0$ and all the significant boundary-layer structure is on the western wall, it follows that the interior pressure field must satisfy the condition $p = 0$ on $x = x_e$.[2] This means that $P_n(x_e) = 0$ in (3.17), and the interior solution is determined by (3.19). For negative slopes, the situation is more complex. For strong negative slope the only boundary layer on the eastern wall is the quasi-barotropic modified Munk layer. The portion of the interior solution that is z independent [corresponding to the first term in (3.19)] is *locally* determined by the modified Sverdrup relation (3.16).

[2] Or more generally $\partial p/\partial y = 0$.

The remaining terms in the series (3.19) are each orthogonal to the z independent structure of the Munk layer, and hence, the Munk layer cannot assist in satisfying the boundary conditions for the higher modes. Hence

$$P_n(x_e) = 0, \quad n > 0, \tag{4.29}$$

for these modes. Thus in this case as well, the interior solution (3.19) with $P_n(x_e) = 0$ is also valid.

The interior solution is only modified in the range $-1 < B^{-1} < 0$ (weak negative bottom slope). Since the baroclinic modes for the interior $\phi_n(z)$ are not each orthogonal to the baroclinic modes in the boundary-layer representation (although both are orthogonal to unity), the matching becomes analytically quite complex.

We have therefore chosen to approach the calculation of the flow by numerically integrating Eqs. (2.1) to (2.4) with the addition of the lateral diffusion terms described in section 2. For the ranges $B^{-1} > 0$, $B^{-1} < -1$, we have compared our solution for v with the interior solution (3.19) generated by the normal-mode analysis. We have always found excellent agreement for the interior, which encourages our belief that the numerical calculation is adequately resolved. For the case of weak negative slope, we can present only the numerical solution. However, we are able, on the basis of the preceding discussion, to completely anticipate the key qualitative features of the solution.

5. Results

Equations (2.1), (2.2), (2.3), and (2.4) were integrated in the region $-H \leq z \leq 0$, $x_w \leq x \leq x_e$. In the case of the meridional momentum equation and the density equation, horizontal mixing terms $A(\partial^2 v/\partial x^2)$ and $\kappa_H(\partial^2\rho/\partial x^2)$ were added to the respective equations to allow satisfaction of the full boundary conditions. The new equations are identical to (4.2) but for the full variables rather than boundary-layer variables. We anticipate that for the cases, $B^{-1} > 0$ and $B^{-1} < 1$ (either positive slope or strong negative slope) where no eastern boundary layers are possible, the interior solution (3.19) with $P_n(x_e) = 0$ should obtain. We use them both as a check of our numerical solution and as a control on the accuracy of the boundary-layer decomposition.

The upwelling w_* is chosen as

$$w_* = KW_* e^{-s(x_e - x)/L}, \tag{5.1}$$

where $L = (x_e - x_w)$ and where K is chosen so that the area integral of w_* over the basin is independent of s. When s is zero, the upwelling is zonally uniform. For $s > 0$, the upwelling is strongest on the eastern boundary. Thus,

$$K = \frac{s}{[1 - e^{-s}]}. \tag{5.2}$$

The variables z, x, v are scaled by H, L, and $KW_*(f/\beta H)$, respectively. A key parameter in our study is the stratification parameter [the ratio of terms ③ and ④ in (4.3)],

$$\alpha = \frac{2\kappa\Omega L^2}{H^4 N^2}, \tag{5.3}$$

where Ω is the earth's rotation. For comparison with P92, we present the case judged most relevant, which is $\alpha = 10^{-3}$. This parameter setting will be fixed, as will the horizontal mixing coefficients

$$\frac{A}{2\Omega L^2} = \frac{\kappa_H}{2\Omega L^2} = 5 \times 10^{-8},$$

and we will focus on the behavior of the solution as a function of B.

The momentum, density, and continuity equations were first combined to form a single equation, identical to (4.3) but for the total pressure p. In anticipation of the need for increased horizontal resolution near the eastern and western walls, the following transformation was applied to the zonal coordinate,

$$\sigma = \frac{1}{2}\left[1 + \frac{\sinh\left(\dfrac{2x - 1}{x_0}\right)}{\sinh\left(\dfrac{1}{x_0}\right)}\right], \tag{5.4}$$

where x_0 is a constant that sets the degree of coordinate compression near the walls. The transformed equation was then approximated using standard second-order finite differences from which the pressure was obtained iteratively using an overrelaxation technique. For the results presented below, we used 20 uniformly spaced grid points in z and 200 grid points in x. We chose $x_0 = 0.3$, so according to (5.4), the grid spacing ranged from $\Delta x = 0.0015$ at the walls to $\Delta x = 0.02$ in the interior.

Figures 3 and 4 present our principal results. In each figure, cross sections of values of the (scaled) meridional velocity are given. In Fig. 3, the case of uniform upwelling ($s = 0$) is presented, while in Fig. 4, the upwelling is strongly localized near the eastern boundary ($s = 5$). Each panel within the figure represents a calculation with a different bottom slope, that is, a different value of B. In addition, each panel is itself a sort of triptych, the middle leaf of which shows the interior while the two outer leaves show, with an expanded zonal scale, the solution for v near the western and eastern boundaries. In our scaled units the western boundary is at $x = 0$ and the eastern boundary is at $x = 1$. Isolines of northward velocity are solid; southward velocity is indicated by dashed contours. The contour intervals in Figs. 3 and 4 are stated in the captions.

One important result that appears immediately in these figures is the relative insensitivity of the interior flow to the size of the bottom *slope*. This can be most

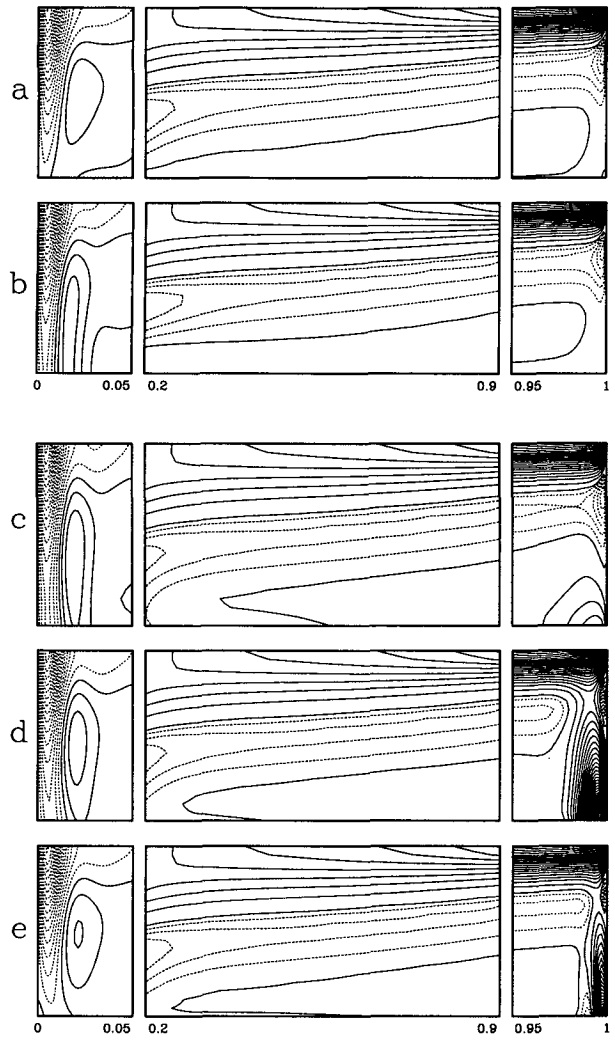

FIG. 3. Isopleths of (scaled) meridional velocity for the case of uniform upwelling ($s = 0$). In each panel, the middle leaf shows the interior flow. The left- and right-hand panels, each with an expanded zonal scale, show the region near the western and eastern boundaries. The range of the zonal coordinate is shown below each panel. Each calculation is done for $\alpha = 10^{-3}$ and for a latitude 30°N. In (a) $B = 0.5$, (b) $B = \infty$, (c) $B = -4$, (d) $B = -2$, (e) $B = -0.5$. Note that for all $(f/\beta H)\partial h/\partial y < 0$, an *eastern* boundary current is evident. Contour intervals are (left panels) 20, (middle panels) 0.2 for $v < 0$, 1 for $v > 0$, (right panels) 0.2 for $v < 0$, 0.5 for $v > 0$.

easily seen by comparing for each s the interior leaves of the triptychs for different B. They are qualitatively similar; certainly more similar for each upwelling distribution than for similar slopes with different upwelling distributions. This point is emphasized in Fig. 5, which shows the profile of $v(z)$ at $x = 0.5$ for nonuniform upwelling ($s = 5$) with $\alpha = 10^{-3}$ for the two cases $B = 100$ (essentially a flat bottom) and $B = -0.5$ (a strong negative bottom slope). These profiles were calculated from the analytical solution for the interior given by (3.19) with $P_n(x_e) = 0$. Over most of the water column the two profiles are indistinguishable even though V_0, by (3.16), are equal and *opposite* for the two cases. Only very near the bottom (within the lower 20% of the water column) is the meridional velocity substantially affected. This is due, we feel, to the relative weakness of the bottom velocity in the flat bottom case (about 10% of the maximum v). As the bottom slope gets larger, regardless of sign, the fluid responds, as can be anticipated by (2.8), by diminishing v. For a given stratification and x scale of forcing, the interior dynamics, governed by (2.10), imposes a limit to the vertical velocity produced at the boundary that can be accepted into the interior. As $\partial h/\partial y$ becomes larger, v must diminish to achieve the required balance in (2.8). This reduction in the velocity at the bottom can be seen in Figs. 3 and 4 as $|B|$ decreases and the zero contour folds in the interior to follow the bottom.

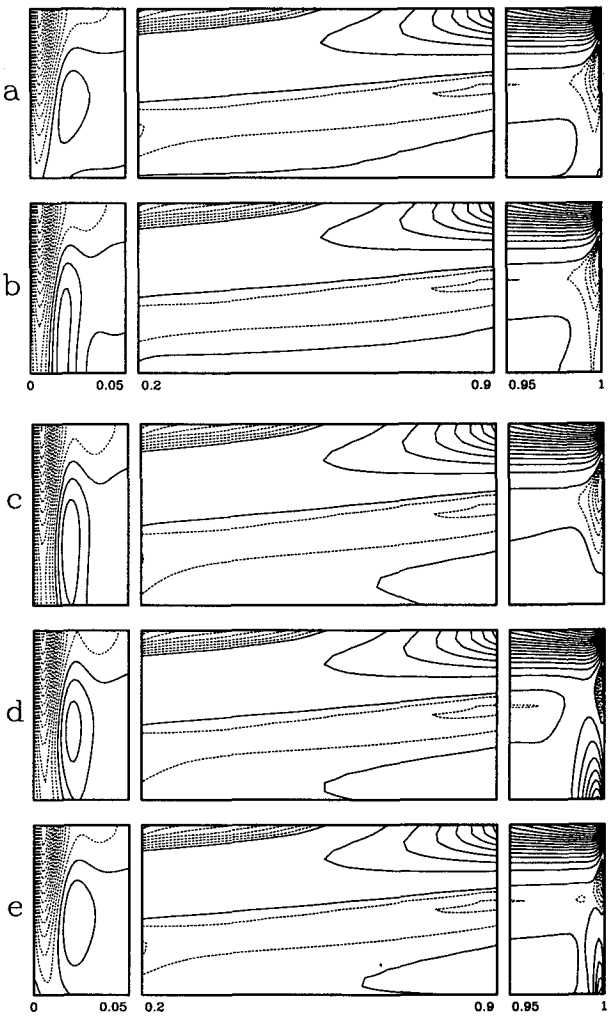

FIG. 4. As in Fig. 3 except that the upwelling is localized near the eastern boundary ($s = 5$). Contour intervals are (left panels) 4, (middle panels) 0.05 for $v < 0$, 0.5 for $v > 0$, (right panels) 0.1 for $v < 0$, 0.5 for $v > 0$.

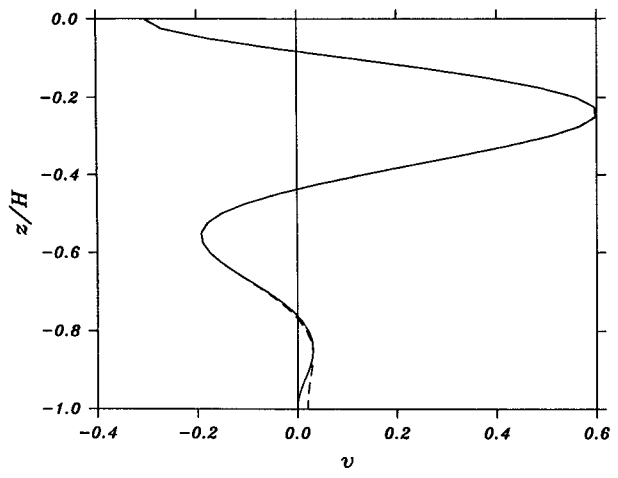

FIG. 5. The meridional velocity for a flat bottom, $B = 100$ (dashed), and a strongly sloping boundary (solid), $B = -0.5$. Note the departure of the two only for $z/H < -0.8$. The calculation is for $\alpha = 10^{-3}$, $\theta = 30°\text{N}$, $s = 5$.

The relative insensitivity of the *interior* velocity to the bottom slope implies that, as in P92, the layering of the interior depends on the zonal variation of the upwelling. This point is perhaps made more clearly in Fig. 6 where the meridional velocity at $x = 0.5$ is compared for the case $s = 0$ and $s = 5$ [with $B = -0.5$, $\alpha = 10^{-3}$, $\theta = 30°\text{N}$, and again using the solution (3.19) with $P_n(x_e) = 0$]. Note the reduction in the *magnitude* of v for the large s since w_* is smaller at $x = 0.5$. Comparing panels (a) and (b) of Fig. 6 emphasizes the much greater layering in the latter when $s > 0$. It is also clear from the figure that although V_0 is negative in both cases, the average of v with depth is clearly still positive. Again, this distinction between V_0 and the vertically averaged v is due entirely to the presence of the bottom slope.

Turning our attention to the boundary-layer panels of our triptychs in Figs. 3 and 4, we see numerical confirmation of one of the most unexpected results of the analysis. This pertains to the appearance of eastern boundary currents for *all* negative slopes, that is, for all $B < 0$ for any value of s, although it is perhaps clearest in the example $s = 0$ where the bottom velocity is strongest.

We have already referred to the wrapping around of the zero velocity contour to run along the bottom when the bottom slope becomes large. For $B < 0$ this withdrawal of the zero contour eastward, forming a bottom tongue of positive meridional velocity can be clearly seen in Fig. (3c). Comparing (3b) (flat bottom) and (3c) (weak negative slope), we see the presence of a bottom-trapped and fairly broad region of northward flow near the eastern boundary (right panel). We identify this with the eastern bottom-trapped boundary-layer mode described in section 4 [e.g., Eqs. (4.13) and (4.18)]. This identification is strengthened by the behavior we observe as the slope is doubled from that in Fig. 3c to Fig. 3d. As expected by the analysis of (4.13b), the bottom-trapped mode becomes taller and narrower as the slope increases in size (i.e., as $|B|$ diminishes). Finally, for $0 > B > -1$, only a tall, thin eastern boundary current, which we identify with the transposed Munk layer, replaces the bottom-trapped mode (Fig. 3e).

It has proven impossible for us, for reasonable parameter settings and reasonable computer resources, to fully achieve the spatial resolution that would allow us to unambiguously distinguish the Munk mode, described by (4.24), and the limiting value of the bottom-trapped mode as $B \to 0$. We content ourselves with the predictions of the asymptotic boundary-layer analysis as a successful qualitative guide. Note that for $s = 5$ the same deep eastern boundary current is present.

The boundary-layer analysis also correctly predicts

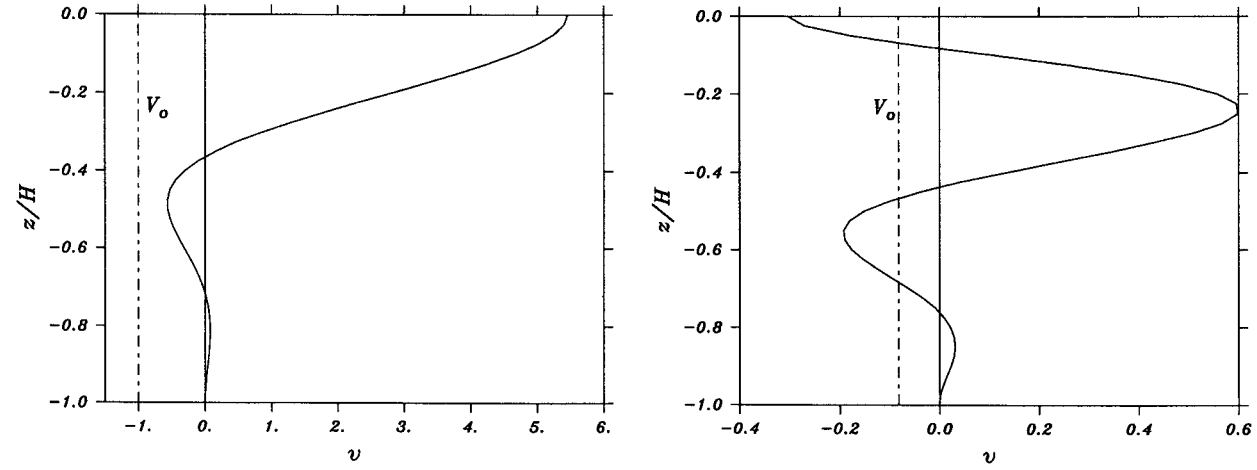

FIG. 6. The meridional velocity at $x = 0.5$ for (a) $s = 0$, (b) $s = 5$. In each case, $B = -0.5$, $\alpha = 10^{-3}$, and $\theta = 30°\text{N}$. Note the greater layering in (b) and the change in the magnitude of v from (a) to (b).

the companion, unexpected result. That is, even when $-1 < B < 0$, so that the overall, barotropically measured, potential vorticity gradient has changed sign and the Munk layer has suffered a transposition from the western wall to the eastern wall, there is still a strong boundary-layer current on the *western* wall. This is consistent with the solution (4.16), which gives rise to a baroclinic boundary layer, due solely to β, that is always valid only near $x = 0$.

For these recirculating solutions, the sense and vertical structure of v in the western boundary layer is determined by the interior flow near $x = 0$. We have seen that for $s = 5$, the interior flow is strongly layered, and this implies that the boundary layer flow will also be layered, thus requiring a substantial contribution from the higher modes in the representation (4.9). Although the boundary-layer correction for each vertical mode decays seaward, the higher vertical modes decay more slowly by (4.16). Thus, the assumption of a thin boundary layer could be violated if the amplitudes $\tilde{A}_n$ do not decay rapidly with increasing n. Qualitatively the numerical solutions (Figs. 3 and 4) suggest that at most only the lowest three or four modes contribute significantly to the western boundary-layer structure, thereby supporting our boundary-layer analysis. However, there is some difficulty in achieving complete quantitative agreement between the numerical results and the analytical asymptotic results, which can be traced to a contamination or leakage into the interior of the effect of the higher boundary-layer modes. This can be appreciated by considering Fig. 7. In Fig. 7a we show two v profiles at $x = 0.5$ for $s = 5$, $B = -0.5$, $\alpha = 10^{-3}$, $\theta = 30°$N. The dashed curve represents the analytical solution as given by (3.19) with $P_n(x_e) = 0$. The solid curve is the full numerical solution obtained by integrating Eq. (4.3) for the total pressure. Comparing the two curves, we find reasonable qualitative agreement between the two methods. However, there is a quantitative discrepancy between the two, that is, the peaks in the analytically derived v exceed those achieved numerically. Figure 7b shows the magnitude of all the terms in (4.3) from the numerical solution as a function of z/H. The term represented by the short dashed curve represents the effect of lateral diffusion of density. Asymptotically, it should be negligible in the middle of the basin. However, given the slow decay of the higher boundary modes, there is a contribution from that term which is 10%–20% of terms ③ and ④, enough to account for the differences in Fig. 7a. Thus, in reality it is probably difficult to achieve an absolutely clean partition between the boundary layer and the interior, although the qualitative nature of the anticipated balances does obtain.

6. Summary and discussion

The introduction of a meridional topographic slope into our continuously stratified, linear model of the abyssal circulation does not substantially alter the nature of the interior flow. We still find, as in P92, that the layering of the interior abyssal flow can be explained as a natural consequence of an eastward intensification of upwelling into the main thermocline of abyssal waters. The principal effect of strongly sloping topography is to further diminish the already weak bottom velocity.

Perhaps the most novel aspect of the analysis is the prediction of *eastern* boundary currents whenever the slope is in the anti-β sense, that is, whenever

$$B = \beta H / f \frac{\partial h}{\partial y}$$

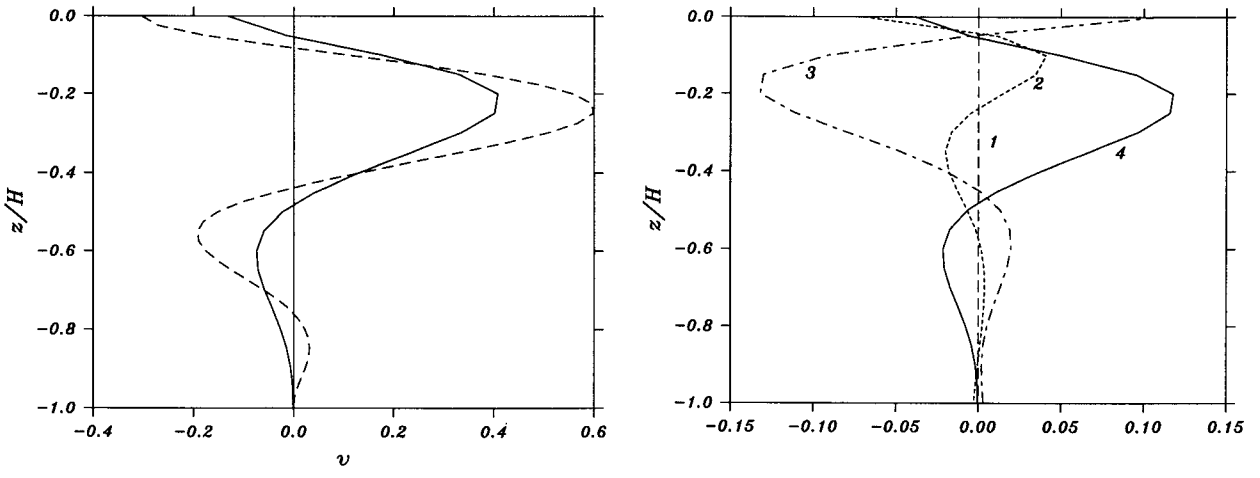

FIG. 7. (a) The numerical (solid curve) and analytical (dashed) solutions for $v(z)$ at $x = 0.5$ with $s = 5$, $B = -0.5$, $\alpha = 10^{-3}$, $\theta = 30°$N. (b) The contributions of the various terms in (4.3). Terms ③ and ④, which are asymptotically dominant in the interior, are given by the dot-dashed and solid curves, respectively. The contribution from the horizontal diffusion of density, term ②, (which should be asymptotically small in the interior) is the short-dashed curve. The effect of the horizontal diffusion of momentum, term ①, is given by the long-dashed curve.

is negative. When the slope is less (in magnitude) than the barotropic critical value which makes $B = -1$, the eastern boundary current is broad and bottom trapped. It becomes narrower and taller as the bottom slopes downward (Northern Hemisphere) more sharply until, at $B = -1$, it metamorphoses into an eastern Munk boundary layer. We consider the absence of a critical slope of great importance and suggest that the dynamical explanation of the observed transposition of the deep abyssal flow in the tropical North Atlantic (Warren 1981) need not require that the slope obtain any particularly steep value.

We emphasize that regardless of the size of the slope, a system of baroclinic, mass transporting boundary currents is always found on the western side of the basin as well.

Obviously, the amount of transport in each boundary current system cannot be usefully calculated with the simple model we have used here. We have exploited the two-dimensional mathematical character of the governing vorticity equation to formulate a somewhat artificial boundary-value problem. Nevertheless, the problem has been illuminating in describing the structure of the expected circulation. To link the net transport to the boundary distribution of deep-water sources demands a three-dimensional model, which is a future step on our agenda.

We are keenly aware of the deficiencies of our model. They include the linearization of the thermodynamics, the assumption of simple eddy viscosity representations, and the limitation of the topography to a broad meridional slope. Nevertheless, some basic aspects of the physics that lead, for example, to the existence of the bottom-trapped eastern boundary current are expected to be robust enough to survive in a more realistic model depending, as they do, on a straightforward interplay between the potential vorticity gradient associated with the lower boundary and the stratification.

It would certainly be of great interest, even within the context of the simple physics of the present model, to extend our study to include topography with a slope in the zonal direction as well. This would make the problem explicitly three-dimensional and tend to twist the direction of the ambient potential vorticity gradient. This would also give an opportunity to link the circulation to its deep-water sources.

Acknowledgments. This research was supported in part by the National Science Foundation under Grant OCE 88-16015 (DC) and the National Science Foundation's Division of Atmospheric Sciences (JP). Computer facilities at the National Center for Atmospheric Research (NCAR) in Boulder, Colorado, were used for the numerical calculations. NCAR is funded by the National Science Foundation.

REFERENCES

Lineykin, P. S., 1955: On the determination of the thickness of the baroclinic layer in the sea. *Dokl. Akad. Nauk. SSSR,* **101,** 461–464.

Pedlosky, J., 1992: On the baroclinic structure of the abyssal circulation. *J. Phys. Oceanogr.,* **22,** 652–659.

Stommel, H., and A. B. Arons, 1960a: On the abyssal circulation of the World Ocean—I. Stationary planetary flow pattern on a sphere. *Deep-Sea Res.,* **6,** 140–154.

——, and ——, 1960b: On the abyssal circulation of the World Ocean—II. An idealized model of the circulation pattern and amplitude in oceanic basins. *Deep-Sea Res.,* **6,** 217–233.

Stommel, H. and G. Veronis, 1957: Steady convective motion in a horizontal layer of fluid heated uniformly from above and cooled non-uniformly from below. *Tellus,* **3,** 401–407.

Warren, B. A., 1981: Deep circulation of the world ocean. *Evolution of Physical Oceanography, Scientific Surveys in Honor of Henry Stommel,* Bruce A. Warren and Carl Wunsch, Eds., The MIT Press, 6–41.